Mapping finite-fault slip using spatial correlation between seismicity and point-source Coulomb failure stress change

Anthony Lomax*[1]

[1]ALomax Scientific, Mouans-Sartoux, France
*Corresponding author: anthony@alomax.net

Supplementary Material

This PDF file includes:

Figure S1-12

Text S1

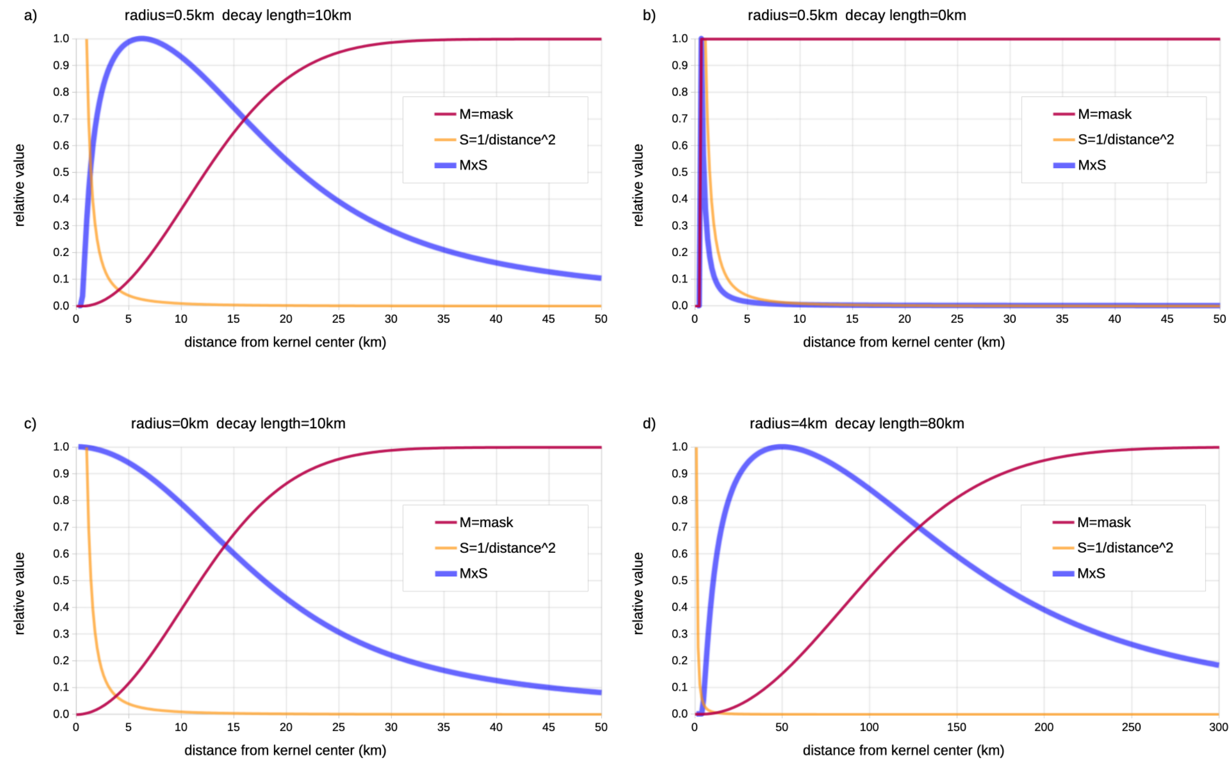

Figure S1. Masking functions for point-source, ΔCFS kernel grids. For the specified zero mask radius, R_m, and decay length, L_m, each panel shows the relative values of the mask function (M; Equation 3 in the main text), an effective envelope of unmasked ΔCFS (S), and the product MxS representing an effective envelope of the masked ΔCFS kernel grid. A $1/r^2$ function, where r is distance, is used for S to account for the product of the $1/r^3$ decay of stress due to a dislocation source in an elastic medium (Okada 1992) and a factor r for the increase in average number of cells containing seismicity with distance, assuming seismicity concentrates on planar surfaces in the study volume. a) R_m = 0.5 km and L_m = 10 km as used for the analysis of the three sequences in the main text. This kernel gives a smoothly masked, ΔCFS kernel grid MxS at larger distances with highest values around L_m, while MxS drops rapidly to zero at small distances to avoid numerical artifacts due to gridding and to suppress uninformative recovery of high slip potential close to each aftershock. b) R_m = 0.5 km and L_m = 0 km to illustrate not using a decay length, which gives a box-car mask beyond R_m and a delta-like function at R_m for the masked ΔCFS kernel grid MxS. This kernel grid would produce uninformative slip potential maps that are very similar to the aftershock distribution. c) R_m = 0 km and L_m = 10 km to illustrate not using a mask radius, which gives a masked ΔCFS kernel grid MxS that is peaked towards zero distance. This kernel would also produce slip potential mainly following the aftershock distribution, as for the kernel shown in b). d) R_m = 4 km and L_m = 80 km as used for the analysis of the larger scale, 2023 Kahramanmaraş, Turkey (Türkiye), earthquake sequence presented in Text S1 in this document.

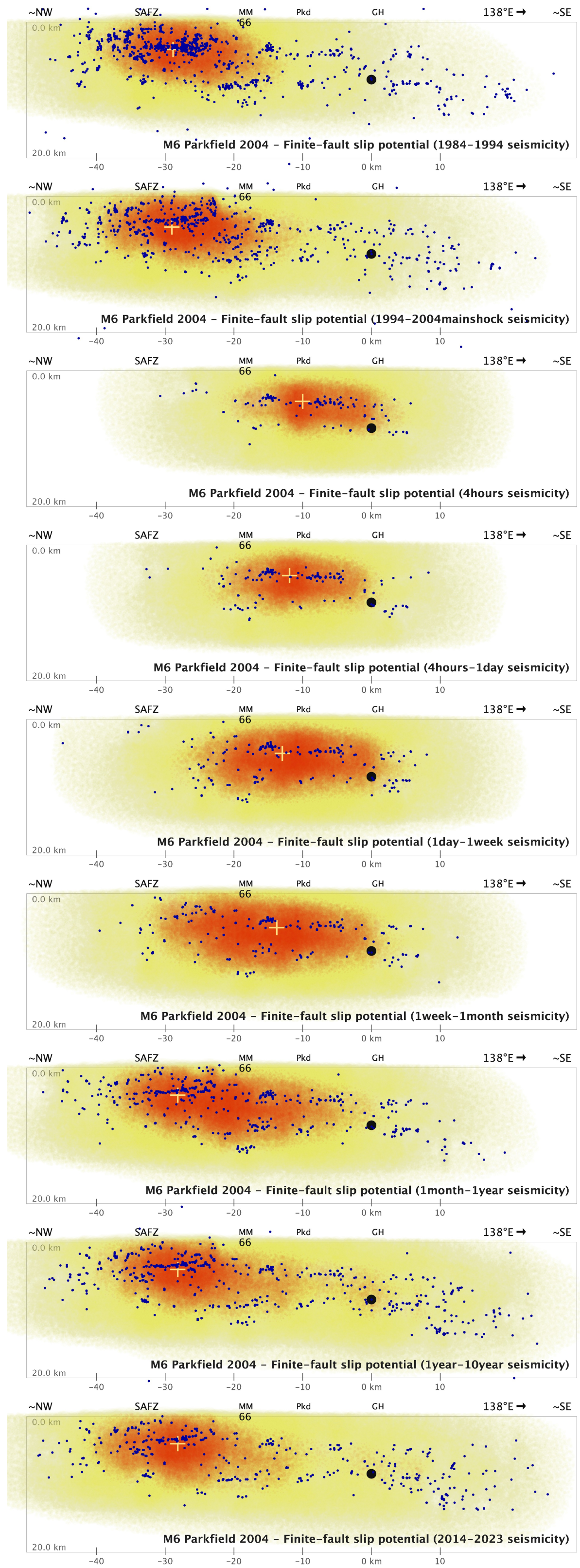

Figure S2. Potential slip maps along the SAF for seismicity in a contiguous set of time windows around the 2004 Parkfield sequence. Maps labelled with date pairs show potential slip for aftershocks (blue dots) between those dates, those labelled with time spans show potential slip for that span after the 2004 mainshock origin. The 2004 mainshock is indicated by the large black dot. Correlation is performed with a ΔCFS kernel for vertical, right-lateral strike slip point-source and receiver faults (main text Figure 1). The relative amplitude of the seismicity-stress finite-faulting field is shown as a 3D density cloud in tones of yellow for portions of the field with normalized correlation < 0.5 and in red for the high-potential portions of the field with normalized correlation ≥ 0.5. Field values are plotted in 3D for each grid cell as transparent disks with radius increasing with correlation value; higher color saturation indicates higher correlation and/or deeper volumes of high correlation. The fields are not clipped to the convex hull of the seismicity, but fading of the fields towards the limits of the plots may be an artifact of lack of seismicity outside the plot and not absence of potential slip. The 1966 Parkfield mainshock epicenter (McEvilly et al. 1967) is indicated by “66”, other abbreviations are: SAFZ – San Andreas fault zone, MM – Middle Mountain, Pkd – Parkfield, GH – Gold Hill.

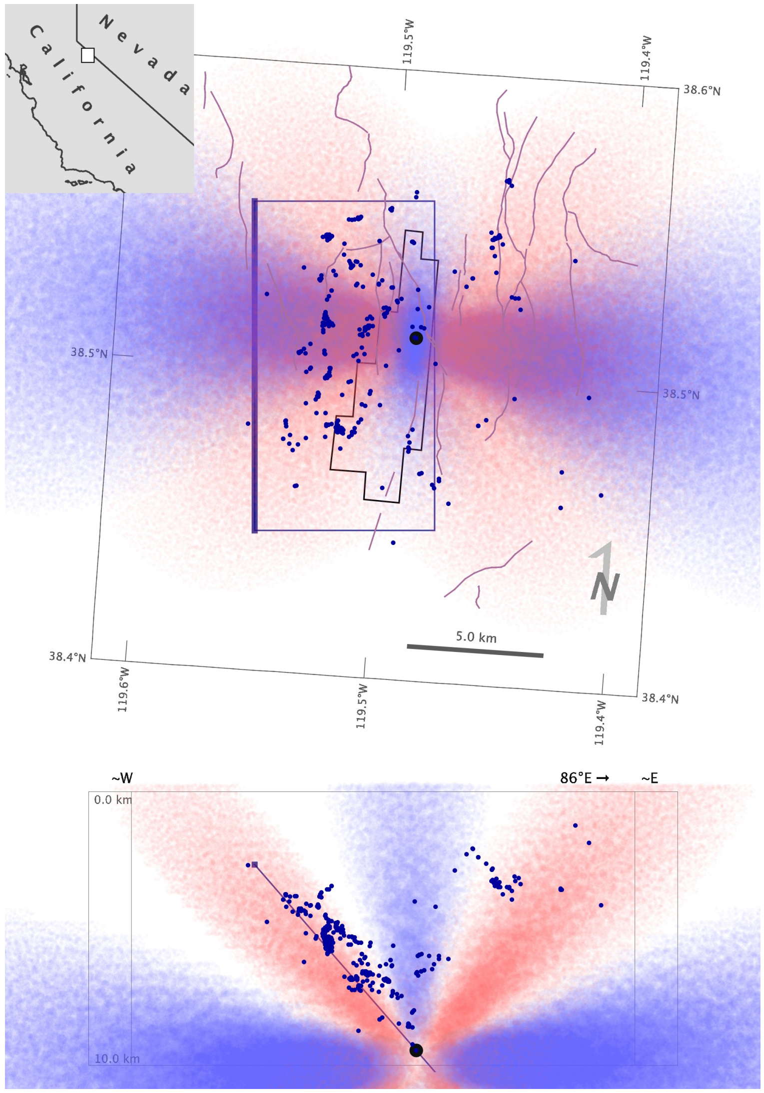

Figure S3. Point-source ΔCFS field (red positive; blue negative) for east-dipping, normal slip source and receiver faults corresponding the geometry of the 2021, Mw 6.0 Antelope Valley sequence. Blue dots show 4 days of aftershocks after the 2021 mainshock (large black dot). Gray rectangle with thick line on upper edge shows orientation of east-dipping, NSL rCMT fault plane, positioned to intersect the relocated mainshock hypocenter and with arbitrary upper and lower depth limits. Purple lines show faults from the USGS Quaternary fault and fold database for the United States.

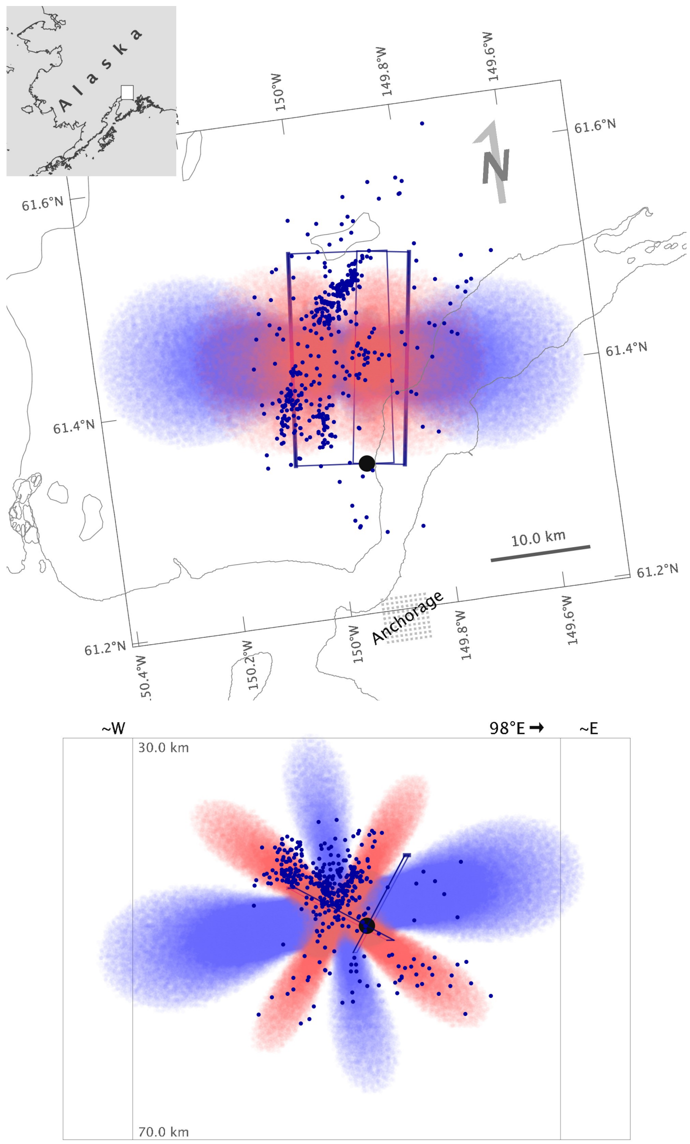

Figure S4. Point-source ΔCFS kernel field (red positive; blue negative) for the normal-faulting, USGS-WCMT mechanism as source and receiver faults corresponding to the west-dipping plane of the USGS-WCMT mechanism for the geometry of the 2018, Mw 7.1 Anchorage sequence. Blue dots show 1 day of aftershocks after the 2018 mainshock (large black dot). Gray rectangles with thick line on upper edge shows orientation of east- and west-dipping USGS-WCMT fault planes, positioned to intersect the relocated mainshock hypocenter and with arbitrary upper and lower depth limits.

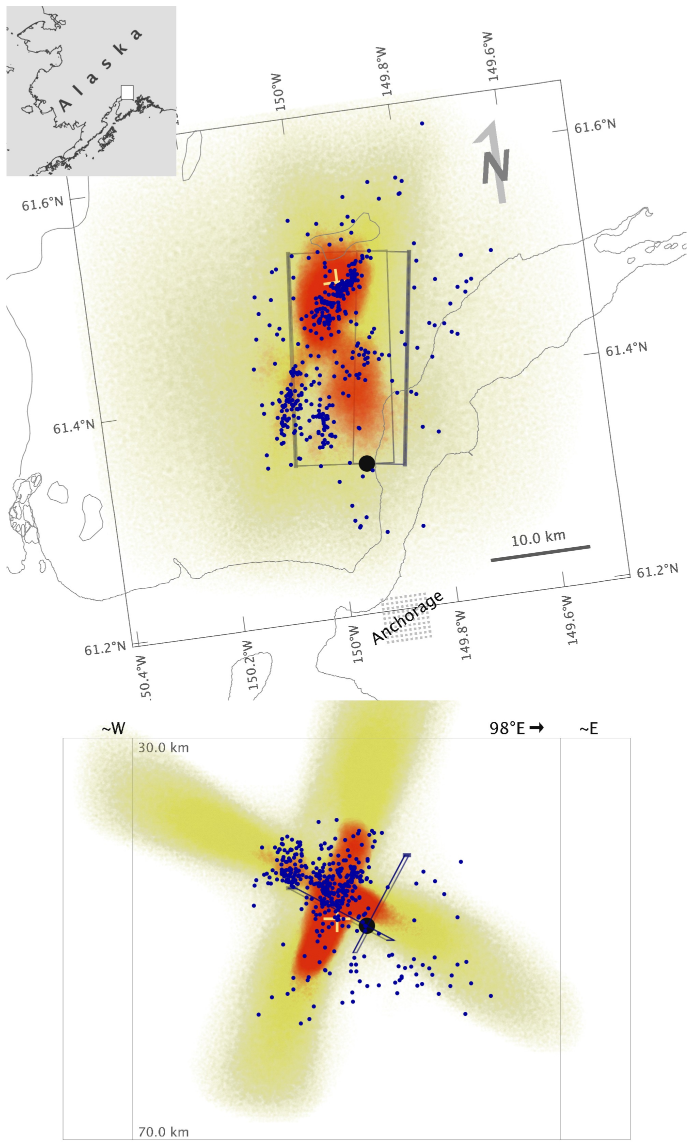

Figure S5. Seismicity-stress, 3D finite-faulting potential slip maps for east-dipping receiver faults inferred from the first 1 day of aftershocks (blue dots) after the 2018 Mw 7.1 Anchorage, Alaska mainshock (large black dot). Map (upper) and profile (lower) views are rotated to the strike of the neutral axis (8°E) of the USGS-WCMT mainshock mechanism (gray rectangles with thick line on upper edge, positioned to intersect the relocated mainshock hypocenter and with arbitrary length and upper and lower depth limits). Correlation is performed with a ΔCFS kernel for the normal-faulting, USGS-WCMT mechanism point-source and for receiver faults corresponding to the east-dipping fault of the USGS-WCMT. The relative amplitude of the seismicity-stress finite-faulting field is shown as a 3D density cloud in tones of yellow for portions of the field with normalized correlation < 0.5 and in red for the high-potential portions of the field with normalized correlation ≥ 0.5, the yellow cross shows the peak value in this field. Field values are plotted in 3D for each grid cell as transparent disks with radius increasing with correlation value; higher color saturation indicates higher correlation and/or deeper volumes of high correlation.

Text S1. Application of seismicity-stress imaging to larger earthquakes and multi-segment rupture

The seismicity-stress procedure can be applied to larger earthquakes and events with complicated, multi-segment fault rupture. Some complications are that multiple source fault mechanism are required when the mainshock rupture involves segments with different orientations or slip directions, or involves a curving fault, and multiple receiver faulting mechanisms may be required to represent diverse aftershock mechanisms. Here we summarize a simplified, preliminary investigation of seismicity-stress imaging of the 2023 Mw 7.8 and Mw 7.5 Kahramanmaraş, Turkey (Türkiye), earthquake sequence (e.g., Goldberg *et al.* 2023; Karabulut *et al.* 2023) where we include a range of source fault orientations, but not all likely receiver fault mechanisms. A comprehensive examination of seismicity-stress imaging of large earthquake rupture and development of relevant algorithms and tools is left to future work.

To apply seismicity-stress imaging in a simplified way to each of the 2023 Turkey mainshocks we use point-source ΔCFS kernels with the same source and receiver faulting mechanism (left-lateral, strike-slip), but generating suites of such kernels by varying the strike angle. The first, Mw 7.8 mainshock involved sinistral rupture along ~300 km of the East Anatolian fault (EAF). To allow recovery of source slip along this long, curving fault segment, we generate left-lateral, strike-slip point-source ΔCFS kernels with strikes ranging from azimuth N200°E to N250°E with a step of 5°. The second, Mw 7.5 mainshock involved sinistral rupture along ~100 km of the Çardak fault for which we generate left-lateral, strike-slip point-source ΔCFS kernels with strikes within +/-10° of the USGS Mww fault plane strike (N277°E) closest to that of the fault, giving an azimuth range from N267°E to N287°E, with a step of 5°. All kernels have a zero mask radius, R_m, of 4.0 km and large decay length, L_m, of 80 km due to the large scale of the sequence (Figure SX1). For aftershock seismicity we use the multi-scale high-precision catalog of Lomax (2023), selecting events in the ~9 hours between the two mainshocks for imaging the first, Mw 7.8 mainshock, and events in the 9 hours after the second, Mw 7.5 mainshock for its rupture imaging.

Figure S6 shows the seismicity-stress results for the two 2023 mainshocks presented with a view that facilitates comparison with previous slip models for the two earthquakes (e.g., Barbot *et al.* 2023, their fig. 6; Goldberg *et al.* 2023, their fig. 5; He *et al.* 2023, their fig. 3; Jia *et al.* 2023, their fig. 1; Melgar *et al.* 2023, their fig. 2; Xu *et al.* 2023, their fig. 3; Zhao *et al.* 2023, their fig. 7; Magen *et al.* 2024, their fig. 6). Most notably, the seismicity-stress imaging recovers high-potential slip concentrated in 3D along the likely causative fault structures for each event, even for the case of the second, Mw 7.5 mainshock where the aftershock seismicity is highly dispersed to the east of the main Mw 7.5 rupture and along the EAF to the east and south.

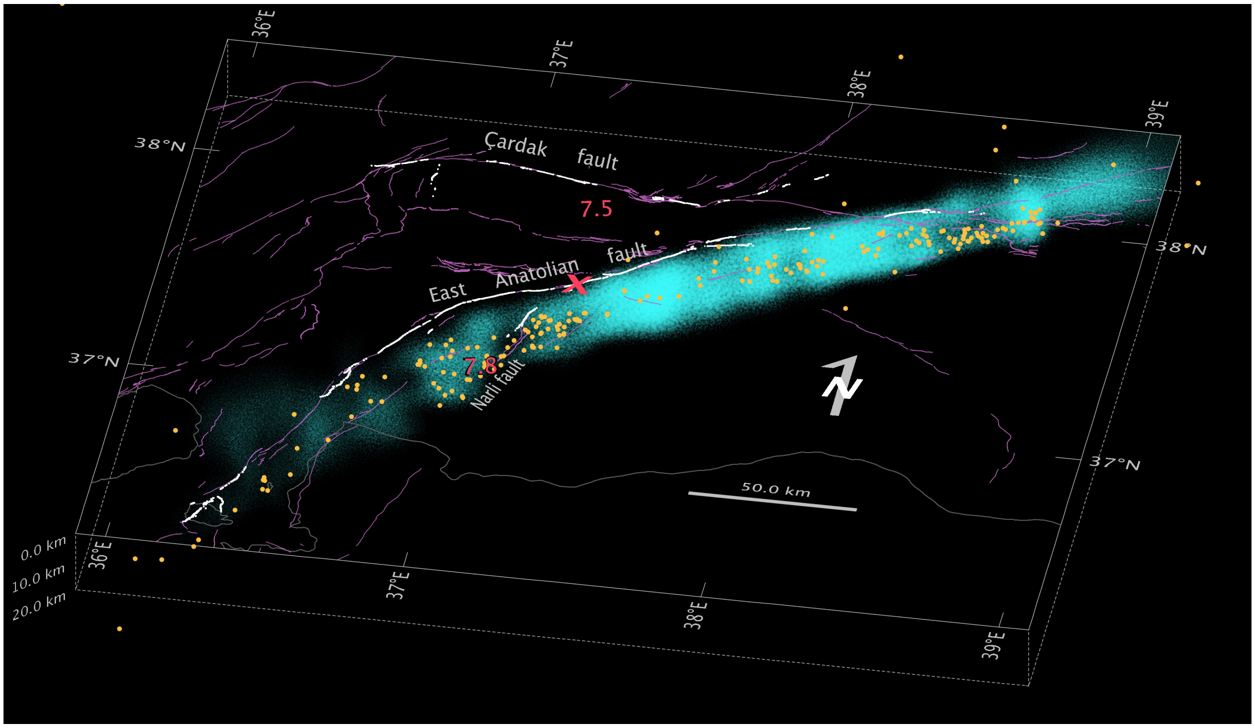

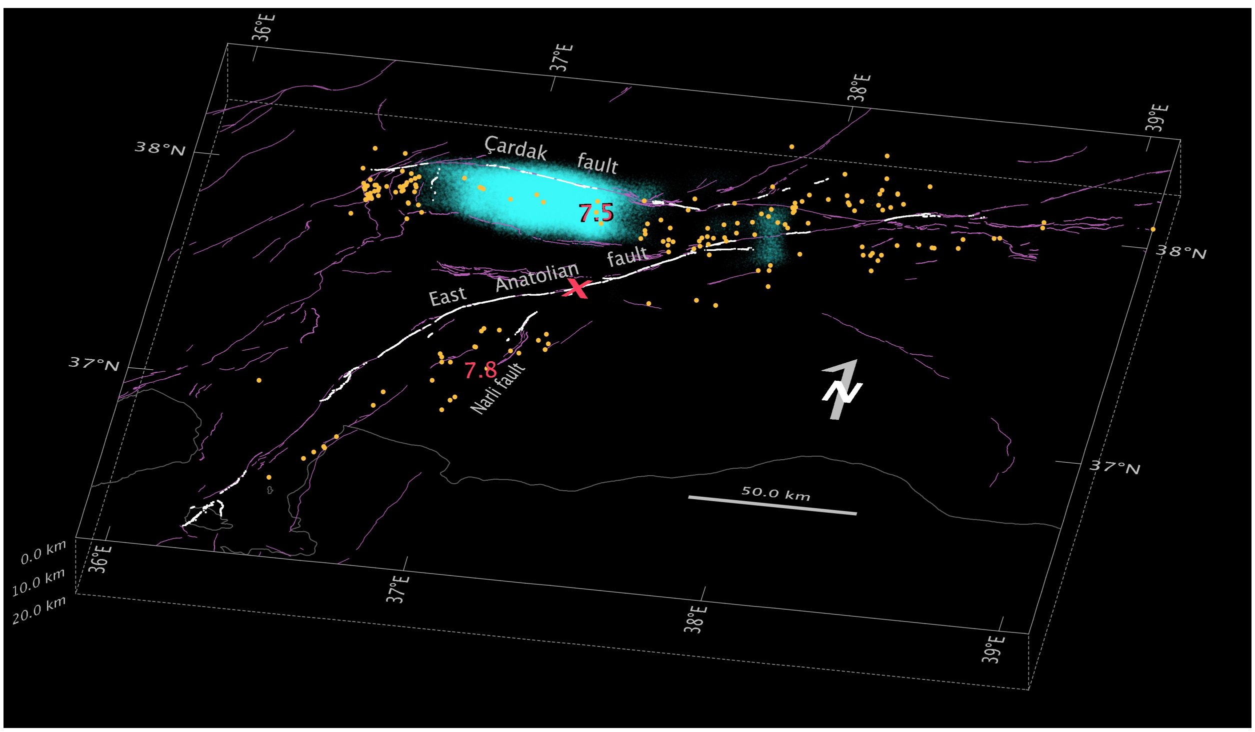

Figure S6. Seismicity-stress imaging of the 2023 Kahramanmaraş, Turkey (Türkiye) earthquake doublet using 9 hours of aftershock seismicity for each event. The figure presents a view in orthographic projection facilitating comparison with previous slip models for the two earthquakes. The relative amplitude of the seismicity-stress finite-faulting fields for the first, Mw 7.8 mainshock (upper panel) and the second, Mw 7.5 mainshock (lower panel) are shown as a 3D density clouds (cyan) for the high-potential portions of the field with normalized correlation ≥ 0.5. Yellow dots show aftershock seismicity (Lomax 2023) for the ~9 hour period after each mainshock used for analysis. Purple lines show mapped surface faults (Emre et al. 2018); white lines show mapped surface ruptures (Reitman et al. 2023); red numbers indicate hypocenter location and magnitude for the two mainshocks; the red X indicates the area where the EAF and the Narli splay-fault converge.

In further detail, the seismicity-stress results agree well with the previous slip models for the distribution of slip and location of areas of larger slip. For the first, Mw 7.8 mainshock, there is very good agreement for the position of highest-slip patches along ~100 km of the EAF to the northeast of the zone where the Narli splay-fault hosting the Mw 7.8 hypocenter reaches the EAF. High seismicity-stress slip farther northeast along the EAF just north of latitude 38° may correspond to high slip in the same area found by Barbot et al. (2023), one of the only previous models that extends this far northeast. There is indication of sparse, smaller patches of low amplitude seismicity-stress slip along the southwestern ~200 km stretch of the EAF correspond to similar features in some or all of the cited previous models, however an oblique orientation of some of these patches and apparent faulting complexity in this area (Okuwaki *et al.* 2023) suggests complete seismicity-stress imaging in this area requires inclusion of additional receiver fault orientations.

For the second, Mw 7.5 mainshock, high slip to the west of the hypocentral area along > 50 km of the Çardak fault, and possible low amplitude slip to the northeast of the hypocenter correspond to similar features in some or all of the cited previous models. Some slip into the westernmost portion of the Çardak fault and branch faults is suggested in the seismicity-stress slip potential, but this area is dominated by extensional aftershock faulting mechanisms (Güvercin 2024) which are not explicitly modeled in this current, preliminary analysis.

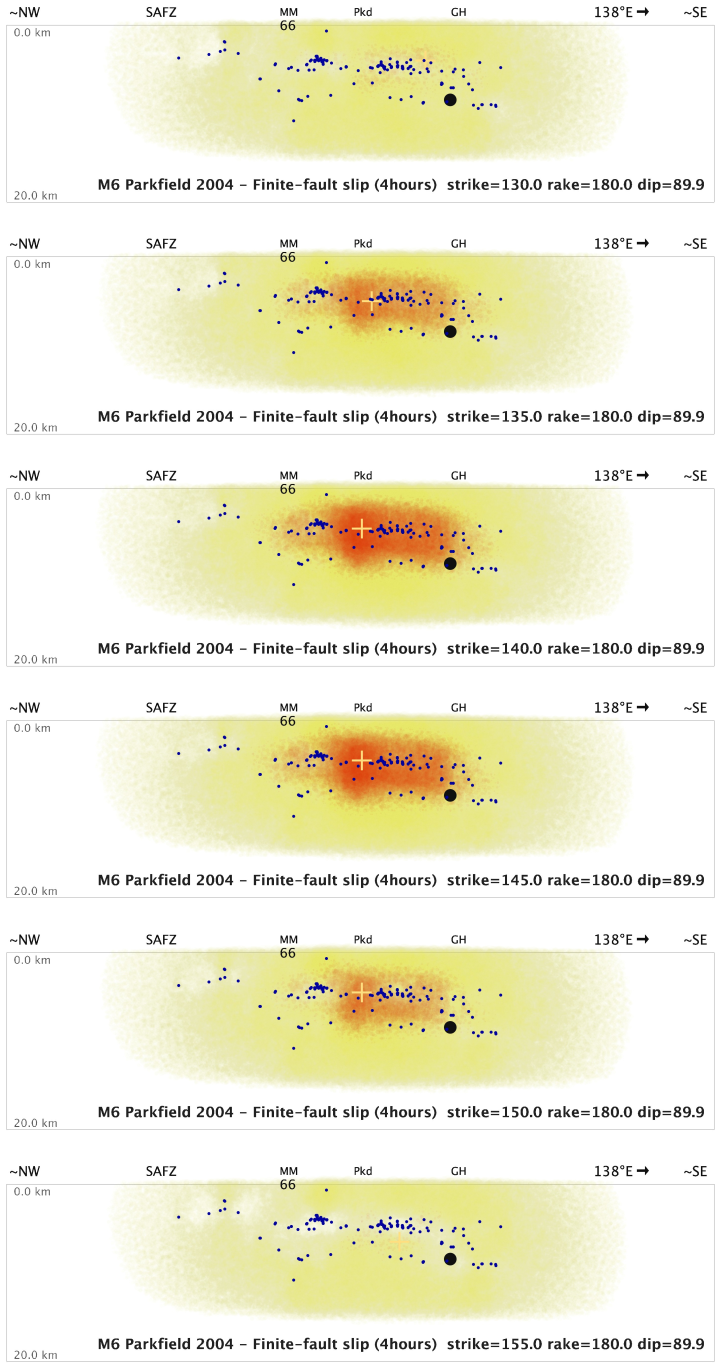

Figure S7. Potential slip maps along the SAF for seismicity for the 2004 Parkfield sequence with variation in source and receiver fault strike around the 140° value used for analysis in this study (main text Figure 3). Map elements as in Figure 3 in the main text. The used strike is specified in the label in each panel. The relative potential slip for all maps is normalized to the peak in the strike 140° map. The slip maps change notably in intensity by not overall form with a +/-10° change in strike. The asymmetry in the variation around 140° is due to the small, counter-clockwise rotation of the positive lobes of the ΔCFS kernel relative to the strike of source fault (see main text Figure 1).

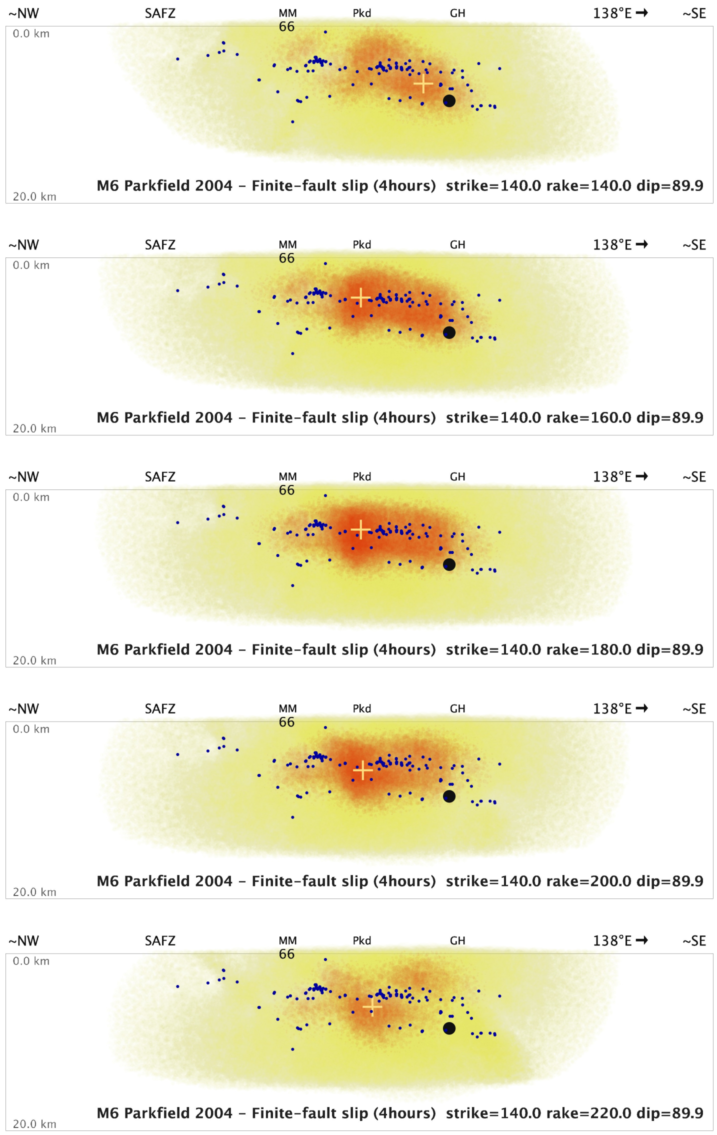

Figure S8. Potential slip maps along the SAF for seismicity for the 2004 Parkfield sequence with variation in source and receiver fault rake around the 180° value used for analysis in this study (main text Figure 3). Map elements as in Figure 3 in the main text. The used rake is specified in the label in each panel. The relative potential slip for all maps is normalized to the peak in the rake 180° map. The slip maps change notably in intensity and in form with a +/-20-40° change in rake.

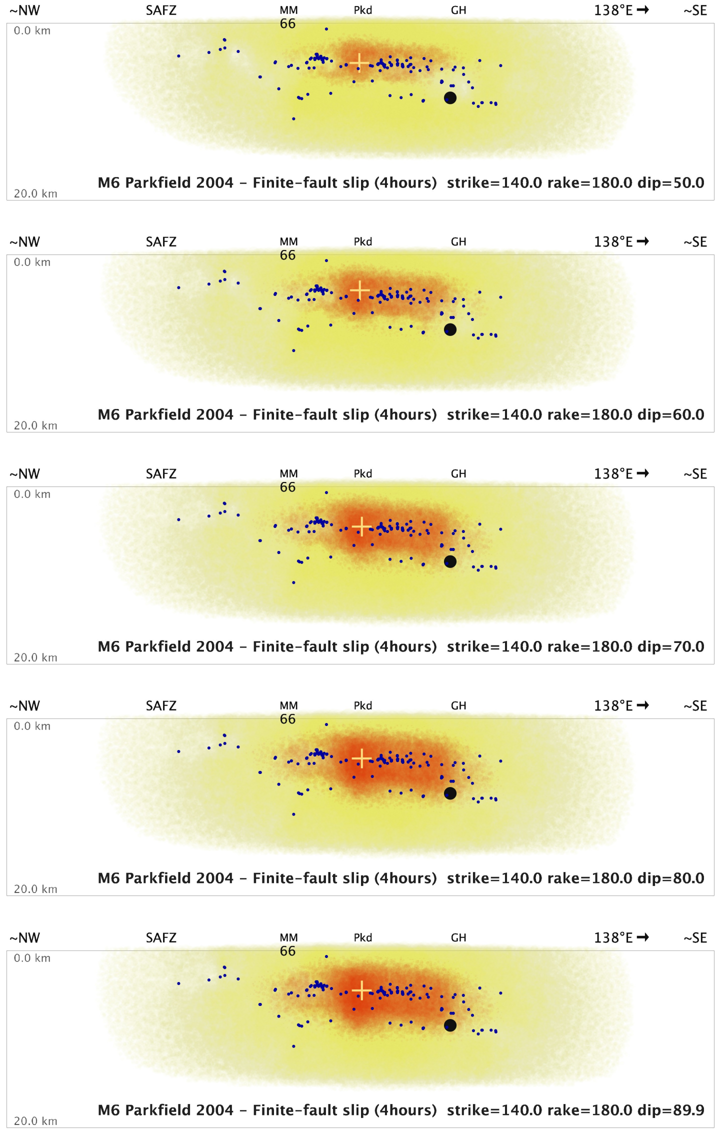

Figure S9. Potential slip maps along the SAF for seismicity for the 2004 Parkfield sequence with variation in source and receiver fault dip up to the 90° value (implemented as 89.9°) used for analysis in this study (main text Figure 3). Map elements as in Figure 3 in the main text. The used dip is specified in the label in each panel. The relative potential slip for all maps is normalized to the peak in the dip 90° map. The slip maps change slightly in intensity but little in form with a -40° change in dip.

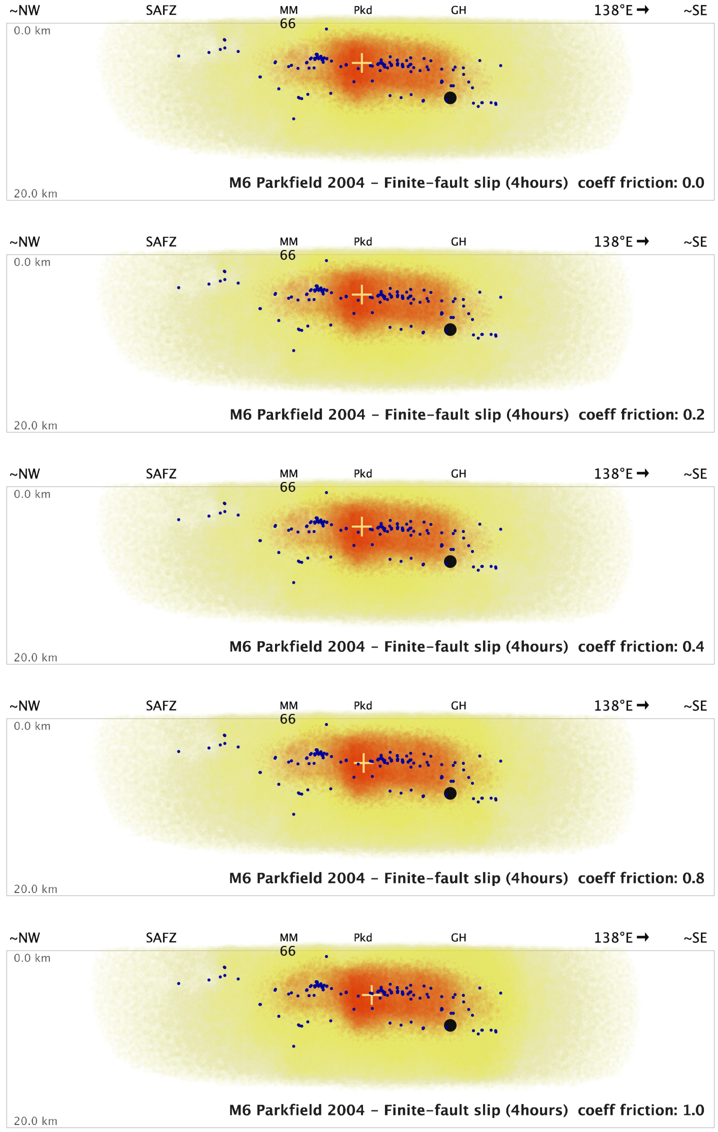

Figure S10. Potential slip maps along the SAF for seismicity for the 2004 Parkfield sequence with variation in effective coefficient of friction, μ', (main text Equation 1) around the μ' = 0.4 value used for analysis in this study. Map elements as in Figure 3 in the main text. The used μ' is specified in the label in each panel. The relative potential slip for all maps is normalized to the peak in the μ' = 0.4 map. The slip maps change very slightly in form and in the position of the slip peak with change in μ'.

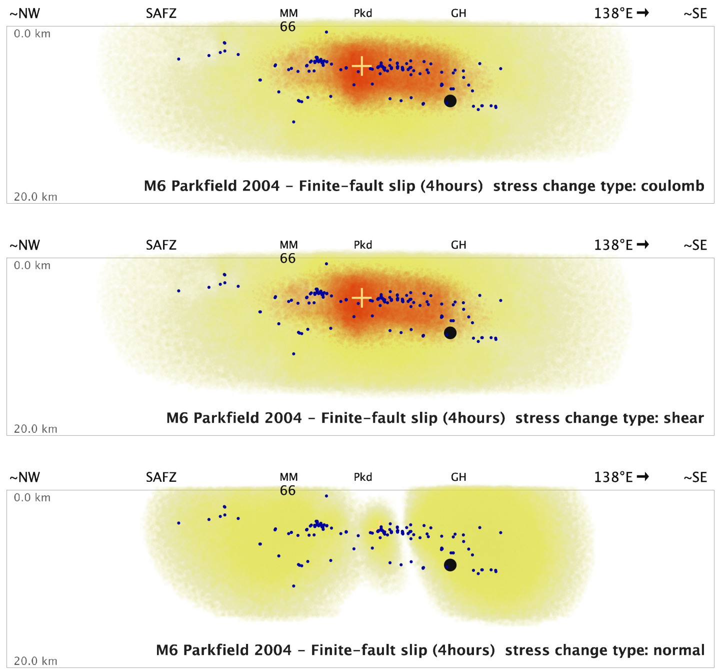

Figure S11. Potential slip maps along the SAF for seismicity for the 2004 Parkfield sequence with variation in stress type used to generate the point-source kernel. Map elements as in Figure 3 in the main text. The used stress type is specified in the label in each panel: *coulomb* (Equation 1 in the main text), *shear* (the first term on the right of Equation 1 in the main text) or *normal* (the second term on the right of Equation 1 in the main text); stress type *coulomb* is used for analyses in this study (e.g., main text Figure 3). The relative potential slip for all maps is normalized to the peak in the stress type *coulomb* map. There are only very minor differences in the stress type *shear* slip map relative to *coulomb* since for the Parkfield strike-slip geometry almost all aftershocks fall along a line parallel to the maximum of the positive shear lobes, while there is effectively no slip imaged using stress type *normal* since the positive normal lobes are perpendicular to the trend of aftershocks (c.f., King *et al.* 1994, their fig. 2a). In cross-correlation of the kernel with the seismicity, aftershocks parallel to a positive lobe produce a strong, constructive sum to total slip.

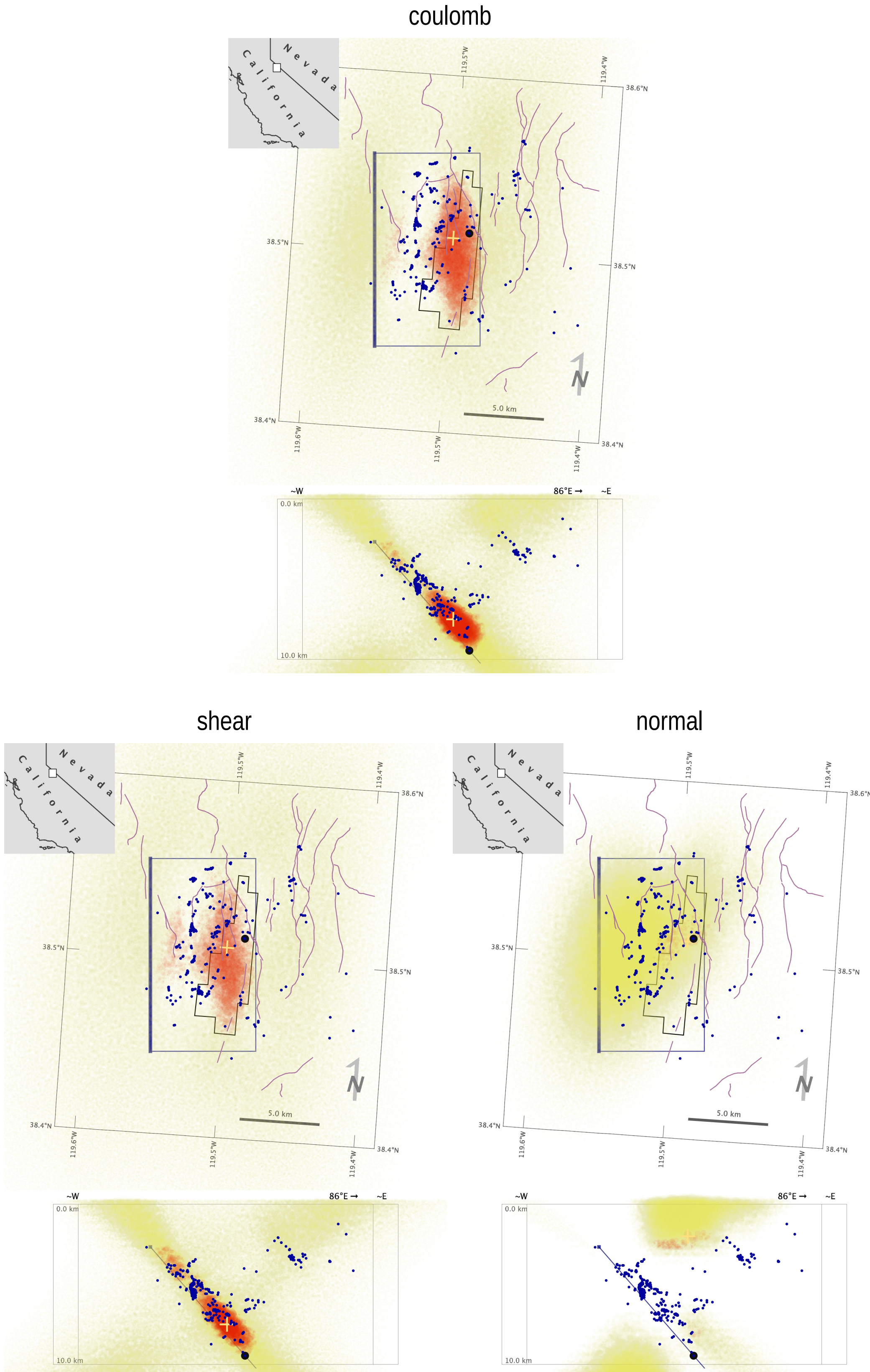

Figure S12. Potential slip maps from seismicity for the 2021, Mw 6.0 Antelope Valley sequence with variation in stress type used to generate the point-source kernel. Map elements as in Figure 5 in the main text. The used stress type is specified for each panel: *coulomb*, *shear* or *normal*, as defined in Figure S11. The relative potential slip for all maps is normalized to the peak in the stress type *coulomb* map. There are small differences in the stress type *shear* slip map relative to *coulomb*, including a reduced amplitude of the main, high-potential slip patch and increased amplitude in the secondary, shallow patch to the west. The stress type *normal* map, however, shows almost no high-potential slip, especially around the likely fault plane and aftershock seismicity, but the *normal* kernel must still perturb the *shear* kernel lobes enough to account for the difference in *coulomb* and *shear* maps.

References

Barbot, S., Luo, H., Wang, T., Hamiel, Y., Piatibratova, O., Javed, M.T., Braitenberg, C., *et al.*, 2023. Slip distribution of the February 6, 2023 Mw 7.8 and Mw 7.6, Kahramanmaraş, Turkey earthquake sequence in the East Anatolian Fault Zone. *Seismica*, **2**. doi:10.26443/seismica.v2i3.502

Emre, Ö., Duman, T.Y., Özalp, S., Şaroğlu, F., Olgun, Ş., Elmacı, H. & Çan, T., 2018. Active fault database of Turkey. *Bull Earthquake Eng*, **16**, 3229–3275. doi:10.1007/s10518-016-0041-2

Goldberg, D.E., Taymaz, T., Reitman, N.G., Hatem, A.E., Yolsal-Çevikbilen, S., Barnhart, W.D., Irmak, T.S., *et al.*, 2023. Rapid Characterization of the February 2023 Kahramanmaraş, Türkiye, Earthquake Sequence. *The Seismic Record*, **3**, 156–167. doi:10.1785/0320230009

Güvercin, S.E., 2024. 2023 Earthquake Doublet in Türkiye Reveals the Complexities of the East Anatolian Fault Zone: Insights from Aftershock Patterns and Moment Tensor Solutions. *Seismological Research Letters*. doi:10.1785/0220230317

He, L., Feng, G., Xu, W., Wang, Y., Xiong, Z., Gao, H. & Liu, X., 2023. Coseismic Kinematics of the 2023 Kahramanmaras, Turkey Earthquake Sequence From InSAR and Optical Data. *Geophysical Research Letters*, **50**, e2023GL104693. doi:10.1029/2023GL104693

Jia, Z., Jin, Z., Marchandon, M., Ulrich, T., Gabriel, A.-A., Fan, W., Shearer, P., *et al.*, 2023. The complex dynamics of the 2023 Kahramanmaraş, Turkey, Mw 7.8-7.7 earthquake doublet. *Science*, **381**, 985–990, American Association for the Advancement of Science. doi:10.1126/science.adi0685

Karabulut, H., Güvercin, S.E., Hollingsworth, J. & Konca, A.Ö., 2023. Long silence on the East Anatolian Fault Zone (Southern Turkey) ends with devastating double earthquakes (6 February 2023) over a seismic gap: Implications for the seismic potential in the Eastern Mediterranean region. *Journal of the Geological Society*, **0**, jgs2023-021, The Geological Society of London. doi:10.1144/jgs2023-021

King, G.C.P., Stein, R.S. & Lin, J., 1994. Static stress changes and the triggering of earthquakes. *Bulletin of the Seismological Society of America*, **84**, 935–953. doi:10.1785/BSSA0840030935

Lomax, A., 2023, June 28. Precise, NLL-SSST-coherence hypocenter catalog for the 2023 Mw 7.8 and Mw 7.6 SE Turkey earthquake sequence., Zenodo. doi:10.5281/zenodo.8089273

Magen, Y., Baer, G., Ziv, A., Inbal, A., Nof, R.N., Hamiel, Y., Piatibratova, O., *et al.*, 2024. Fault Coalescence, Slip Distribution, and Stress Drop of the February 2023 Southeast Türkiye Earthquakes from Joint Inversion of SAR, GNSS, and Burst Overlap Interferometry. *Seismological Research Letters*. doi:10.1785/0220230271

Melgar, D., Taymaz, T., Ganas, A., Crowell, B.W., Öcalan, T., Kahraman, M., Tsironi, V., *et al.*, 2023. Sub- and super-shear ruptures during the 2023 Mw 7.8 and Mw 7.6 earthquake doublet in SE Türkiye, EarthArXiv. Retrieved from https://eartharxiv.org/repository/view/5071/

Okada, Y., 1992. Internal deformation due to shear and tensile faults in a half-space. *Bulletin of the Seismological Society of America*, **82**, 1018–1040. doi:10.1785/BSSA0820021018
Okuwaki, R., Yagi, Y., Taymaz, T. & Hicks, S.P., 2023. Multi-Scale Rupture Growth With Alternating Directions in a Complex Fault Network During the 2023 South-Eastern Türkiye and Syria Earthquake Doublet. *Geophysical Research Letters*, **50**, e2023GL103480. doi:10.1029/2023GL103480
Reitman, N.G., Briggs, R.W., Barnhart, W.D., Hatem, A.E., Thompson Jobe, J.A., DuRoss, C.B., Gold, R.D., *et al.*, 2023. Rapid Surface Rupture Mapping from Satellite Data: The 2023 Kahramanmaraş, Turkey (Türkiye), Earthquake Sequence. *The Seismic Record*, **3**, 289–298. doi:10.1785/0320230029
Xu, L., Aoki, Y., Wang, J., Cui, Y., Chen, Q., Yang, Y. & Yao, Z., 2023. The 2023 Mw 7.8 and 7.6 Earthquake Doublet in Southeast Türkiye: Coseismic and Early Postseismic Deformation, Faulting Model, and Potential Seismic Hazard. *Seismological Research Letters*. doi:10.1785/0220230146
Zhao, J.-J., Chen, Q., Yang, Y.-H. & Xu, Q., 2023. Coseismic Faulting Model and Post-Seismic Surface Motion of the 2023 Turkey–Syria Earthquake Doublet Revealed by InSAR and GPS Measurements. *Remote Sensing*, **15**, 3327, Multidisciplinary Digital Publishing Institute. doi:10.3390/rs15133327